PCCP

PAPER

View Article Online
View Journal | View Issue

Cite this: *Phys. Chem. Chem. Phys.*, 2026, **28**, 1645

NMR relaxometry probes solvent-polarity-dependent molecular interactions in stimuli-responsive lyogels

Muhammad Adrian, *[a] Kathrin Marina Eckert, [bh] M. Raquel Serial, [ac] Artyom Tsanda, [de] Lukas Rennpferdt, [g] Stefan Benders, [ah] Hoc Khiem Trieu, [g] Tobias Knopp, [def] Irina Smirnova [bh] and Alexander Penn [ah]

Stimuli-responsive gels demonstrate macroscopic changes upon exposure to external stimuli, offering potential for the development of adaptive chemical reactors. Early investigations into hydrogels established that crosslinked polymer networks experience reversible volume phase transitions, with temperature, pH, and solvent composition governing swelling and shrinking dynamics. Although hydrogels behavior in aqueous environments has been extensively characterized, lyogels that incorporate organic solvents remain comparatively underexplored, despite their potential for enhanced chemical compatibility and functional versatility. Here, we investigate how solvent polarity and crosslinking density govern the swelling behavior, pore formation, and molecular-scale dynamics of poly(*N*-isopropylacrylamide)-based lyogels. Using a combination of swelling measurement, scanning electron microscopy, and multiscale NMR relaxometry and diffusometry, we demonstrate that solvent polarity fundamentally alters lyogel structure and dynamics. Lyogels swollen in a high-polarity solvent exhibits macroporous networks and slower solvent exchange rates, whereas a low-polarity solvent induces shrinkage, denser microstructures, faster solvent exchange rates, and stronger surface interactions. These results establish a mechanistic framework linking thermodynamic affinity, solvent dynamics, and microstructural confinement to macroscopic gel responsiveness. This framework provides guidance for tailoring lyogels in dynamic environments, with potential applications in adaptable and tunable chemical reactors.

Received 21st October 2025,
Accepted 3rd December 2025

DOI: 10.1039/d5cp04032a

rsc.li/pccp

1. Introduction

Stimuli-responsive gels have emerged as a versatile class of materials that exhibit macroscopic changes in response to external stimuli. Their adaptive behavior makes them highly attractive for applications in flow control systems,[1] sensor applications,[2] and functionally adaptable-tunable or SMART reactors.[3,4] Earlier studies from Tanaka *et al.*[5–8] demonstrated that polymer networks, such as hydrogels, can undergo volume phase transition in response to environmental changes. Since then, extensive studies have shown that external stimuli, such as temperature, pH, electric fields, and chemical species, can induce the swelling and shrinking of such networks.[9,10] Hoare and Kohane[11] later emphasized the importance of tuning solvent–polymer interactions to achieve precise control over material responses.

Gels consist of a three-dimensional polymer network that can retain many times their own mass of solvents within the polymer matrix (Fig. 1). Based on the solvent absorbed in the matrix, a distinction can be made between hydrogels, which contain water, and lyogels, which contain organic solvents. The use of organic solvents not only broadens chemical compatibility but also enables the introduction of diverse functional groups, enhancing responsiveness and allowing property tuning for specific applications.[12]

[a] *Institute of Process Imaging, Hamburg University of Technology, Hamburg, Germany. E-mail: muhammad.adrian@tuhh.de*
[b] *Institute of Thermal Separation Processes, Hamburg University of Technology, Hamburg, Germany*
[c] *Department of Process and Energy, Delft University of Technology, Delft, The Netherlands*
[d] *Institute for Biomedical Imaging, Hamburg University of Technology, Hamburg, Germany*
[e] *Section for Biomedical Imaging, University Medical Center Hamburg-Eppendorf, Hamburg, Germany*
[f] *Fraunhofer Research Institution for Individualized and Cell-based Medical Engineering IMTE, Lübeck, Germany*
[g] *Institute of Microsystems Technology, Hamburg University of Technology, Hamburg, Germany*
[h] *United Nations University Hub on Engineering to Face Climate Change at the Hamburg University of Technology, United Nations University Institute of Water, Environment and Health, Hamburg, Germany*

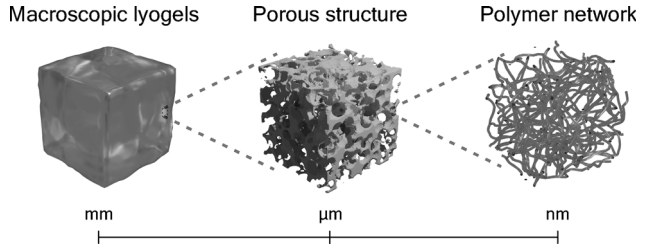

Fig. 1 Schematic illustration of lyogels spanning from macroscopic to microscopic scale. Unlike hydrogels, lyogels incorporate organic solvents instead of water.

In this study, we focus on lyogels synthesized from *N*-isopropylacrylamide (NIPAM), a thermoresponsive polymer with amphiphilic character arising from hydrophilic amide groups and hydrophobic isopropyl side chains.[13–15] This dual affinity controls molecular-scale solvent–polymer interactions to macroscopic swelling behavior, making NIPAM-based lyogels an ideal platform for studying solvent effects across a range of polarities.

Understanding the fundamental physical and chemical principles that occur at the microstructural level during swelling and shrinking is crucial for optimizing lyogels for practical applications.[16] Despite significant progress in understanding stimuli-responsive hydrogels, the mechanisms by which solvent–polymer interactions and microstructural dynamics control the macroscopic lyogel behavior remain incompletely understood. To address this gap, a multiscale characterization approach is required. Swelling measurements provide valuable data on macroscopic changes and kinetics.[16,17] In comparison, advanced microscopic techniques such as (environmental) scanning electron microscopy (ESEM/SEM), transmission electron microscopy (TEM), or micro-computed tomography (μCT) offer insights into microstructural properties.[18–20] Most of these microscopic techniques require dried samples or demand extensive methodological development to be adapted for use of gels in the solvated state.[18,19] As a result, correlating the structures obtained using these methods with solvent-induced properties is often not straightforward. Moreover, small-angle X-ray scattering (SAXS) can complement these techniques by providing structural and morphological information on wet gels, but it is a highly resource-intensive method.[21,22]

Another useful technique is nuclear magnetic resonance (NMR) relaxometry and diffusometry, which enable non-invasive access into molecular structure dynamics. NMR relaxometry probes relaxation times that are sensitive to molecular motion, confinement, and structural heterogeneity.[23,24] NMR diffusometry, on the other hand, probes molecular displacement and transport properties, providing insight into translational motion over micrometer length scales. The diffusion measurement is based on the pulsed-field gradient spin-echo (PGSE) technique introduced by Stejskal and Tanner,[25] which was later complemented by Cotts through the development of the pulsed-field gradient stimulated echo (PGSTE) method,[26] enabling quantification of diffusion in heterogeneous environments. Many studies have adapted NMR techniques to elucidate solvent dynamics and microstructural features such as binding interactions within polymer networks, while tailoring these methods to meet diverse experimental conditions and application-specific requirements.[27–32] For example, D'Agostino *et al.*[33,34] investigated swelling-induced structural changes in gelatin gels and molecular motion in emulsion gels using NMR relaxometry and diffusometry, while Knörgen *et al.*[35] examined swelling and diffusion in hydrogels through ^{1}H NMR imaging. Despite these advances, to the best of the author's knowledge, no similar investigations have been performed in lyogels.

To investigate polymer and solvent dynamics at the molecular level, ^{1}H NMR relaxometry and diffusometry were complemented by other analytical techniques to develop a framework for understanding solvent–polymer interactions in NIPAM-based lyogels with varying solvent polarities. A multi-technique approach is essential for characterizing poly(*N*-isopropylacrylamide) (pNIPAM) lyogels in various solvents and capturing their structural complexity. Macroscopic swelling measurements provide initial insights into how solvent polarity and crosslinker concentration influence the lyogel's bulk behavior, while SEM allows for visualization of changes in the porous microstructure across solvents. At the molecular scale, NMR relaxometry and diffusometry enable mechanistic interpretation of solvent–polymer interactions and transport phenomena within the lyogel matrix.

2. Experimental

2.1. Lyogel synthesis and preparation

Lyogels were synthesized by dissolving 2.175 g of NIPAM with *N,N′*-methylenebisacrylamide (MBA) in 23 g of deionized water, followed by nitrogen degassing for 30 min. Sodium metabisulfite (SMBS, 2.5 mg) and ammonium persulfate (APS, 2.5 mg), were each dissolved in 1 mL of deionized water and subsequently added to the mixture. Lyogels with varying crosslinker concentrations (0.007–0.050 g crosslinker per g monomer) were prepared using MBA as the crosslinker. The resulting lyogel monoliths were cast in 10 mL syringes sealed with parafilm. After polymerization, the gels were cut into cylinders approximately 1.5 cm in height and thoroughly washed with deionized water for three days.

Lyogel synthesis was performed *via* a two-step solvent exchange protocol designed to probe the influence of solvent polarity. Ethanol (EtOH) was selected as a representative high-polarity solvent, while butyl acetate (BuAc) was the low-polarity solvent. For EtOH-based lyogels, the samples underwent three successive solvent exchanges followed by equilibration for 48 h at 25 °C. In the case of BuAc-based lyogels, an additional solvent exchange step was introduced to transition from EtOH to BuAc. This transition induced shrinkage, which altered the final gel structure and properties.

2.2. Standard gel characterization

In addition to the NMR-based analysis, the macroscopic swelling was determined by calculating the degree of swelling (*Dos*):

$$Dos = \frac{m_{\text{gel, equilibrated}}}{m_{\text{dried polymer}}} \quad (1)$$

For this analysis, the equilibrated lyogel was weighed and subsequently dried at 40 °C (± 0.1 °C) for 48 h to obtain the mass of the dried polymer.

Furthermore, the porous structure of the lyogel was characterized using SEM. Prior to imaging, the samples were dried with supercritical CO_2. The lyogels were sealed in bags of filter paper and dried in a custom-built autoclave with a volume of 250 mL. The drying was performed for 3 h at 60 °C and 125 bar to preserve their native pore architecture. The samples were then cut open and sputtered with a thin carbon layer of approximately 10 nm. The SEM analysis was conducted using a Zeiss Supra VP55 equipped with a cold field emission gun and in-lense detector for imaging. The measurements were performed using an acceleration voltage of 5.00 kV. Supercritical drying was employed to preserve the native structure.[18] It must be emphasized that the SEM images only reflect the structure of the dried samples, which could often exhibit a certain shrinkage upon CO_2 drying. Therefore, no absolute conclusions about the pore structure in the wet gels can be drawn from them. Only trends of the different structure in varying solvents can be inferred from this data. This structural imaging information from SEM analysis was used to correlate with NMR relaxometry and diffusometry, providing insights into the relationship between microstructure and solvent dynamics at the molecular level.

2.3. NMR measurement

Equilibrated lyogels with five distinct crosslinker concentrations, prepared in EtOH and BuAc, were left under ambient conditions for 3 min to facilitate bulk solvent evaporation. Subsequently, the samples were cut to a uniform mass of approximately 20 mg and placed into custom microfabricated glass holders, produced *via* selective laser-induced etching (SLE) (Fig. 2). This holder was inserted into a 5 mm NMR tube and was specifically designed to ensure consistent sample positioning and optimal signal quality.

All NMR experiments were performed using a 60 MHz benchtop spectrometer equipped with a pulsed field gradient system and temperature control maintained at 26 °C (Spinsolve 60, Magritek, Germany). Three key parameters were quantified: (a) transverse relaxation time (T_2) measured using the Carr–Purcell–Meiboom–Gill (CPMG) sequence with an echo time of 300 μs, (b) longitudinal–transverse relaxation correlation (T_1–T_2) measurements performed with an inversion recovery–CPMG (IR-CPMG) sequence using an echo time of 300 μs, and

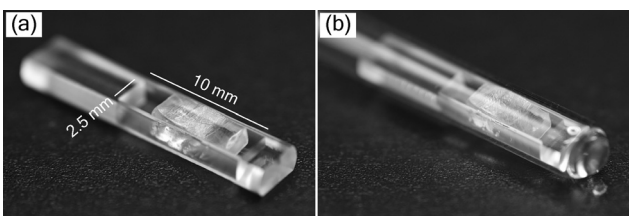

Fig. 2 (a) Glass NMR sample holder with its cavity filled with lyogel, ensuring uniform distribution and (b) final assembly inserted into a standard NMR tube for reproducible sample positioning and measurement.

Table 1 NMR relaxometry parameters that were used to characterize solvent–polymer interactions in lyogels dispersed in EtOH and BuAc

NMR relaxometry	CPMG	IR-CPMG
Echo time [μs]	300	300
Number of echoes	30 000	25 000
Repetition time [s]	15	21
Number of points	32	32
Number of scans	4	4

Table 2 NMR diffusometry parameters used for assessing solvent–polymer interactions of lyogels in EtOH and BuAc

NMR diffusometry	PGSTE
Diffusion time [ms]	80
Gradient pulse duration [ms]	2
Repetition time [s]	15
Max gradient strength [mT m^{-1}]	552
Number of points	16 384
Number of scans	4

(c) self-diffusion coefficient (D) determined using the pulsed gradient stimulated echo (PGSTE) method with a diffusion time (Δ) of 80 ms (Tables 1 and 2). Parameters such as echo time and diffusion time were carefully optimized to account for the time sensitivity of the lyogels. As prior studies report no measurable dependence of PFG attenuation on diffusion times in hydrogel,[33] the present measurements were treated as effectively diffusion-time independent. Dwell time and related acquisition parameters were further optimized to ensure reproducibility and adequate relaxation between scans.

NMR data from three different batches of measurements were processed using custom Python scripts designed to analyze both one- and two-dimensional relaxation and diffusion datasets. Distribution functions of relaxation times from CPMG data were obtained using the inverse Laplace transform (ILT)[36,37] with Tikhonov regularization (α = 0.1). The regularization parameter was selected using L-curve approach[38] (see SI, Fig. S2) to balance between noise suppression and resolution, ensuring the identified peaks represent physically meaningful solvent populations. For methodological consistency, the same regularization parameter was applied to IR-CPMG data. Signal components with amplitudes exceeding 1% of the amplitude-normalized intensity were considered indicative of distinct populations. The diffusion data was processed using monoexponential fitting, assuming that the solvent molecules primarily exhibit free diffusion. To further quantify solvent–polymer interactions, binding dynamics were evaluated by calculating solvent exchange rates (k_{ex}) and standard Gibbs energy of binding ($\Delta_B G^\circ$) at equilibrium state.[39–41] Molecular exchange between two sites involves transitions between environments with different local relaxation properties. Under the slow exchange limit, free and bound solvent populations were resolved based on their characteristic T_2 relaxation times, modeled as:

$$[\text{free solvent}] \underset{[k_{\text{dissociation}}]}{\overset{[k_{\text{binding}}]}{\rightleftharpoons}} [\text{bound solvent}] \quad (2)$$

where [free solvent] and [bound solvent] denote the concentrations of the solvent in the free and bound states and $k_{binding}$ and $k_{dissociation}$ are the binding and dissociation rate constants, respectively. The total exchange rate (k_{ex}) is given by:

$$k_{ex} = k_{binding} + k_{dissociation} \quad (3)$$

and slow exchange conditions were defined by:

$$k_{ex} \leq \frac{1}{T_{2,bound}} + \frac{1}{T_{2,free}} \quad (4)$$

The binding constant (K_B), describing the balance of bound and free solvent, was calculated as:

$$K_B = \frac{[\text{bound solvent}]}{[\text{free solvent}]} = \frac{P_{bound}}{P_{free}} \quad (5)$$

where P_{bound} and P_{free} are the site occupancy of bound and free solvent, respectively. In this regime, the total magnetization relaxation follows a multi-exponential decay:

$$\frac{M(t)}{M_0} = P_{free}e^{-t/T_{2,free}} + P_{bound}e^{-t/T_{2,bound}} \quad (6)$$

where P_{free} and P_{bound} can be determined from the relative amplitudes of the corresponding exponential components:[42]

$$P_{free} = \frac{A_{free}}{A_{free} + A_{bound}}, \quad P_{bound} = \frac{A_{bound}}{A_{free} + A_{bound}} \quad (7)$$

where A is the amplitude of the corresponding component. Finally, standard Gibbs energy of binding $\Delta_B G^\circ$ associated with solvent–polymer binding was determined from K_B:[43,44]

$$\Delta_B G^\circ = -RT \ln K_B \quad (8)$$

where R is the universal gas constant (8.314 J mol^{-1} K^{-1}) and T is the absolute temperature in Kelvin, assuming a room temperature of 20 °C. The NMR measurements were cross-validated with complementary techniques, including swelling measurements and SEM imaging, and were further compared with theoretical models reported from previous studies.[16]

3. Results and discussion

3.1. Standard characterization of lyogels

The macroscopic analysis of the *Dos* reveals solvent-induced shrinkage and the influence of crosslinker concentration on swelling behavior. While pNIPAM lyogels exhibited strong swelling in EtOH, significant shrinkage occured after solvent exchange to BuAc (Fig. 3). A study[16] attributed this effect to the higher polarity of EtOH, which enhances solvent–polymer interactions, in contrast to those observed for BuAc. Furthermore, in the macroscopic analysis, decreasing swelling for increasing crosslinker concentrations could be observed in EtOH and BuAc. This effect was particularly pronounced at higher crosslinker concentrations, where the constrained polymer network restricted solvent absorption, leading to shrinkage. These observations align to previous studies highlighting how solvent polarity and crosslinker concentration affect hydrogel swelling.[5,19,45]

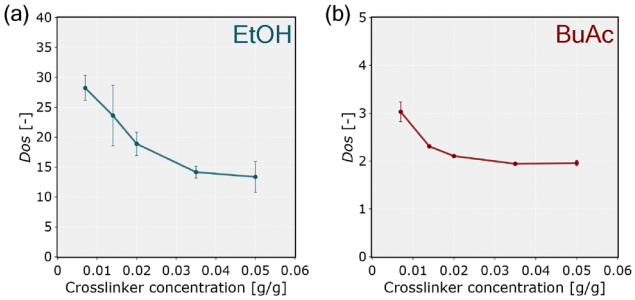

Fig. 3 The degree of swelling (*Dos*) of lyogels in (a) EtOH and (b) BuAc. *Dos* is defined as the ratio of the mass of equilibrated lyogels to the mass of the polymer after drying the equilibrated lyogels.

Table 3 Infinite dilution activity coefficients (IDACs) (γ_i^∞), hydrogen-bonding (E^{HB}), and van der Waals interaction energies (E^{VdW}) for the interactions between NIPAM and pure solvents (EtOH, BuAc), calculated using COSMO-RS model.[16] A lower IDAC value indicates higher solute miscibility with the given solvent, whereas more negative interaction energy values correspond to stronger solute–solvent interactions

Solvent	EtOH	BuAc
$\ln(\gamma_i^\infty)$	0.026	0.813
E^{HB} [kJ mol^{-1}]	−9.91	−1.37
E^{VdW} [kJ mol^{-1}]	−81.19	−83.00

A recent study by Eckert *et al.*[16] utilized COSMO-RS (conductor-like screening model for real solvents)[46] as thermodynamic model to provide a quantitative framework for predicting solvent–polymer interactions based on the molecular structure of the monomers. With this approach, quantitative predictions of activity coefficients, hydrogen bonding, and van der Waals interactions between NIPAM and the two solvents were provided. The model results confirmed that hydrogen bonding interactions prevail in EtOH, while in BuAc, weaker hydrogen bonding is formed (Table 3).

The theoretical calculations were consistent with the observed swelling equilibria. As expected, stronger interactions between the lyogel monomer and the solvent correlated with increased swelling behavior. The COSMO-RS calculations describe bulk properties, but do not account for structural effects, such as steric hindrance within the gel matrix. The calculations were performed under conditions of infinite dilution, representing a single monomer in a bulk solvent. Thus, the model is suitable for assessing component miscibility and predicting bulk thermodynamic properties. The model, however, does not capture surface interactions or structural constraints arising from the polymer network.

Furthermore, the significant differences in the macromolecular structure of lyogels prepared in EtOH compared to BuAc are consistently reflected by the SEM analysis (Fig. 4). While lyogels prepared in EtOH exhibit a macroporous structure, no distinct pore architecture could be identified in lyogels in BuAc based on the SEM analysis. The pore sizes in the BuAc-derived lyogels are significantly smaller and not resolvable by SEM, likely due to the pronounced shrinkage observed under

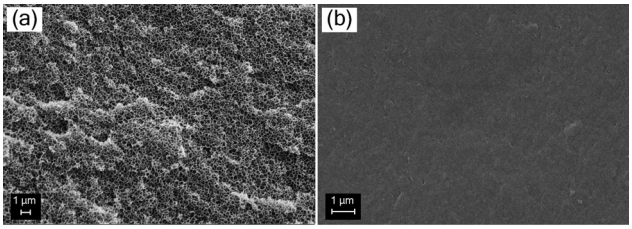

Fig. 4 SEM images pNIPAM-based lyogels prepared in solvents of different polarities. (a) Lyogels treated with EtOH at crosslinker concentration of 0.050 g g^{-1} exhibited a clearly visible porous structure. In contrast, (b) lyogels treated with BuAc at the same crosslinker concentration showed significantly reduced porosity, with no clear pore structure.

these solvent conditions. Consequently, we conclude that a dense and collapsed polymer network is formed in the presence of BuAc.

3.2. NMR relaxometry and diffusometry

Based on solvent thermodynamic interactions with the polymer network and in accordance with previous studies on hydrogels and other porous media,[32,47,48] NMR relaxometry further enables the differentiation of distinct solvent populations within the lyogel matrices. As illustrated schematically in Fig. 5, three distinct solvent populations could be identified within the lyogel: (i) bound solvent, which is strongly attached to polymer side chains, exhibiting severely restricted molecular motion and short T_2 values; (ii) restricted solvent, weakly bound and confined between polymer chains, where partial hindrance of motion results in intermediate T_2 values; and (iii) free solvent, unbound and freely mobile within the interconnected pore space of the polymer matrix, displaying high molecular mobility and long T_2 relaxation times. This classification provides a useful framework for interpreting the relaxation populations obtained from NMR relaxometry and highlights the hierarchical nature of molecular dynamics in lyogels.

Analysis of CPMG relaxation data revealed three distinct T_2 populations in lyogels swollen with EtOH, while only two were identified in lyogels swollen with BuAc (Fig. 6). This finding contrasts the typical observations in other porous media, where

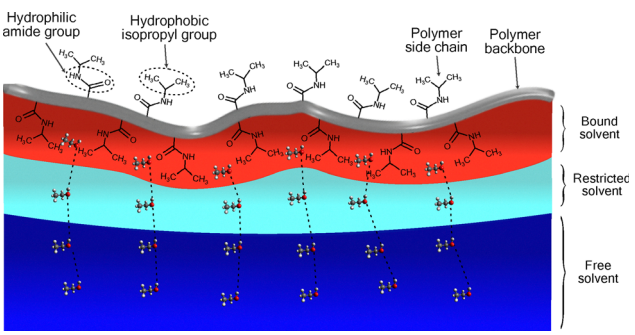

Fig. 5 Schematic illustration of pNIPAM interaction with solvents categorizing them into; bound solvent (where the first solvent interacts with the polymer side chain), restricted solvent (subsequent solvent molecules with limited mobility), and free solvent. Molecular structures used in figures were generated with Avogadro (version 1.2.0).[49]

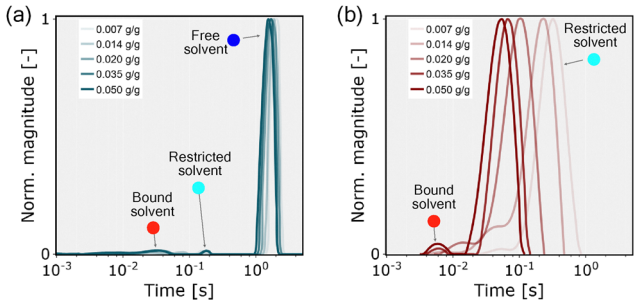

Fig. 6 Laplace inversion of CPMG measurement of lyogels (a) in EtOH and (b) in BuAc. T_2 relaxation times are defined as the time corresponding to the peak signal intensity. The results revealed varying T_2 relaxation times for different types of lyogels based on crosslinker concentrations from 0.007 to 0.050 g g^{-1}. The figure shows amplitude-normalized signal intensity to account for variations in sample weight during measurement.

usually only two solvent populations, free and bound are detected. The presence of a third, intermediate population in lyogels highlights the complex solvent–polymer interaction mechanism unique to gels. The three T_2 populations correspond to (i) free solvent ($T_2 \approx 1$ s), which is highly mobile and experience minimal interaction with the polymer network, detectable only in lyogels swollen with EtOH; (ii) restricted solvent ($T_2 \approx 100$ ms), which is partially confined within the polymer mesh; and (iii) bound solvent ($T_2 \approx 10$ ms), which is closely associated with or interact onto the polymer backbone, exhibiting significantly reduced mobility (Fig. 6).

These relaxation times reflect the degree of confinement and solvent–polymer interactions, with shorter T_2 values corresponding to more restricted, decreased mobility environments (solid-like). Furthermore, an increase in the crosslinker concentration resulted in a systematic decrease in T_2 values across identified populations, with the most pronounced reductions observed in the free solvent fraction of lyogels in EtOH and in the restricted solvent fraction of lyogels in BuAc (Fig. 7a and d). This trend indicates a denser, more compact polymer network, leading to increasingly reduced solvent mobility and enhanced shrinkage of the lyogels. These observations are consistent with earlier studies on crosslinking-dependent swelling and molecular dynamics in hydrogels, where increased crosslinking density reduces network porosity and solvent mobility.[7,27,33]

In addition to T_2 relaxation times, T_1–T_2 correlation maps were examined, from which the T_1/T_2 ratios have been derived (Fig. 7b, c, e and f). The T_1/T_2 ratio serves as a probe for surface relaxation effects, owing to its sensitivity to molecular motion, and is commonly employed as an indicator of surface interaction strength.[50] When molecules interact with a polymer surface, their rotational and translational motion are hindered, resulting in increased T_1/T_2 ratio.[29,51] According to the Bloembergen–Purcell–Pound (BPP) theory,[52] nuclear spin relaxation arises from local magnetic field fluctuations caused by molecular motion, characterized by the correlation time (τ_c). In low-viscosity fluids, where molecular motion is rapid ($\tau_c << 1/\omega_0$, with ω_0 being the Larmor frequency), both T_1 and T_2 are relatively long and of similar magnitude. In confined

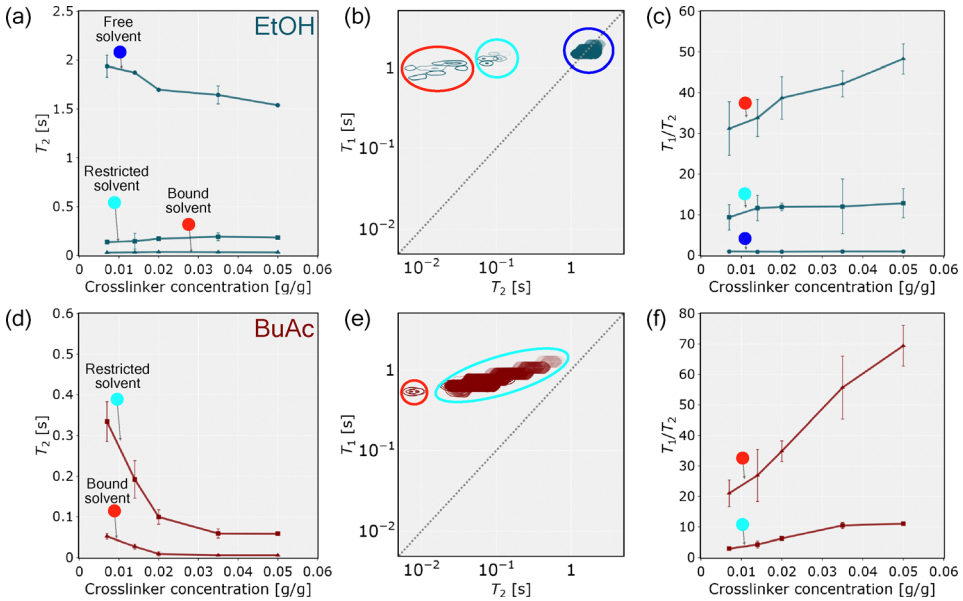

Fig. 7 T_2 relaxation, T_1–T_2 correlation map, and T_1/T_2 ratio of pNIPAM across different crosslinker concentration in EtOH ((a)–(c)) and in BuAc ((d)–(f)). The results reveal distinct solvent populations and their corresponding T_2 relaxation times, which vary depending on the crosslinker concentration of the lyogels. Additionally, differences in solvent polarity influence the surface interactions between solvent and polymer backbone. The blue, cyan, and red circles mark distinct populations corresponding to free solvent, restricted solvent, and bound solvent, respectively.

environments, for example near polymer surfaces, molecular motion becomes restricted, leading to enhanced surface relaxation for both T_1 and T_2, with T_2 exhibiting higher sensitivity due to magnetic susceptibility induced internal field gradients.[53] These gradients shorten T_2 by inducing spin dephasing that further attenuates the signal and increases sensitivity to surface interactions. T_1 is largely unaffected by such internal gradients,[54] leading to increases in the T_1/T_2 ratio in liquids where stronger surface interactions are present. Consequently, a higher T_1/T_2 ratio reflects slower rotational and translational dynamics and stronger molecular interactions with the surrounding matrix.[39] This effect is evident from the measurements, as the free solvent population in EtOH, which exhibits minimal interactions with the polymer surface, remains the least affected, despite a reduction in T_2 relaxation times when crosslinker concentration increases (highlighted by the blue circle in Fig. 7a and c). As an initial step, T_1–T_2 correlation maps were evaluated, which provided further evidence for distinct solvent populations, in agreement with T_2 relaxation profiles (in Fig. 7b and e, blue, cyan, and red circles mark distinct populations corresponding to free solvent, restricted solvent, and bound solvent, respectively). Notably, a free solvent population was observed exclusively in EtOH, as indicated by signal intensity in close proximity to the diagonal line ($T_1 = T_2$), which is characteristic of freely moving solvent with minimal motional restriction (Fig. 7b). The absence of a free solvent in BuAc is attributed to the shrinkage of the polymer network, which expels the free solvent during lyogel shrinkage, leaving only restricted or bound fractions (Fig. 7e). When examining the relaxation time distributions derived from the T_1–T_2 correlation maps, the T_1 distributions are comparatively narrow, whereas the T_2 distributions exhibit pronounced broadening, consistent with previous observations in hydrogels.[55] This difference arises from the distinct sensitivity of the two relaxation mechanisms to molecular motion and structural heterogeneity within the lyogel network.[52] The T_1 relaxation primarily reflects molecular reorientation processes at Larmor frequencies and is therefore less affected by spatial restrictions. In contrast, T_2 relaxation is strongly influenced by slow molecular motions and local magnetic field inhomogeneities caused by pore geometry and solvent–polymer interactions. Consequently, variations in pore size and connectivity within the heterogeneous lyogel matrix lead to a broad distribution of T_2 values, while the T_1 relaxation remains largely invariant across different regions of the lyogels. These observations further confirm the progressive confinement of pores and the enhanced surface interactions, as reflected by the increasing T_1/T_2 ratio with higher crosslinker concentration (Fig. 7c and f).

Comparing lyogels in EtOH and BuAc highlights pronounced differences in their relaxation behavior. Relative to EtOH, lyogels in BuAc exhibit lower T_2 values and predominantly high T_1/T_2 ratios, consistent with more restricted molecular motion and enhanced surface interactions. This difference can be attributed to the smaller pore sizes in BuAc, which result in stronger surface interactions compared to the more macroporous network in EtOH. Referring to the thermodynamic modeling (Table 3), stronger solvent–polymer interactions were predicted in EtOH than in BuAc, which may appear to contradict the interpretation derived from the NMR relaxometry discussed above. Although both approaches consider solvent–polymer interactions, they capture fundamentally different aspects: thermodynamic modeling reflects the bulk properties of the system, whereas NMR relaxometry provides direct insight into the changing interactions at the polymer

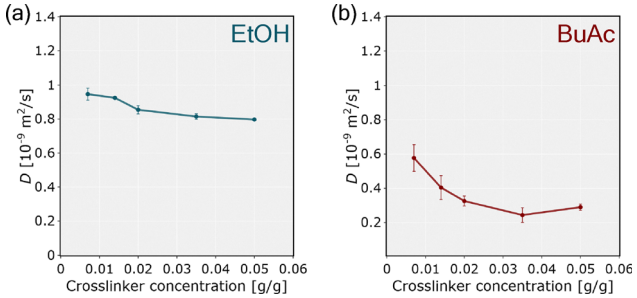

Fig. 8 The effective self-diffusion coefficients (D) of EtOH and BuAc were determined in pNIPAM–based lyogels with crosslinker concentrations ranging from 0.007 to 0.050 g g^{-1}, with the most pronounced decrease observed for BuAc in pNIPAM.

surface. Furthermore, since the COSMO-RS calculations were performed on monomers and oligomers,[16] this technique can only capture a limited impact of the lyogels' structural properties. In contrast, NMR relaxometry enables the analysis of both structural characteristics and solvent to polymer–surface interactions or surface interaction strength.

Since solvent-induced shrinkage influences not only the structural changes but also the diffusive properties of lyogels, the subsequent analysis focuses on the solvent self-diffusion coefficient as a quantitative measure for comparison. The self-diffusion coefficients of bulk EtOH and BuAc were determined by NMR diffusometry, yielding values of 1.11×10^{-9} m^2 s^{-1} and 1.62×10^{-9} m^2 s^{-1}, respectively. The comparison of effective self-diffusion coefficient (D) showed that lyogels in BuAc exhibited higher restriction than those in EtOH (Fig. 8). The larger deviation between the bulk and effective (D) values further evidences that molecular transport within the lyogel matrix is more hindered in BuAc than in EtOH. The results align with the previously determined higher fraction of free solvent in EtOH-based lyogels compared to those in BuAc, as revealed by the ILT analysis (Fig. 6). The lower self-diffusion coefficient in BuAc lyogels is likely attributable to stronger surface interactions and increased microstructural complexity. These factors reduce the accessible bulk volume for diffusion, resulting in a smaller and more constrained porous network, supported by the SEM micrographs (Fig. 4). The observed trends are evident not only when comparing the effects of EtOH and BuAc on the porous structure, but also with increasing crosslinker concentration, indicating a more compact network in highly crosslinked lyogels. These findings are consistent with previous studies on diffusion in polymer networks, where solvent quality, network architecture, or polymer chain dynamics were shown to significantly influence diffusivity.[31,33,56]

3.3. Solvent exchange rate and standard Gibbs energy of binding

Binding dynamics within lyogels were characterized by quantifying solvent exchange rates (k_{ex}) between different populations and by determining the standard Gibbs energy of binding ($\Delta_B G^\circ$) at equilibrium, following the principles outlined in Section 2.3. It is important to note that these analyses are

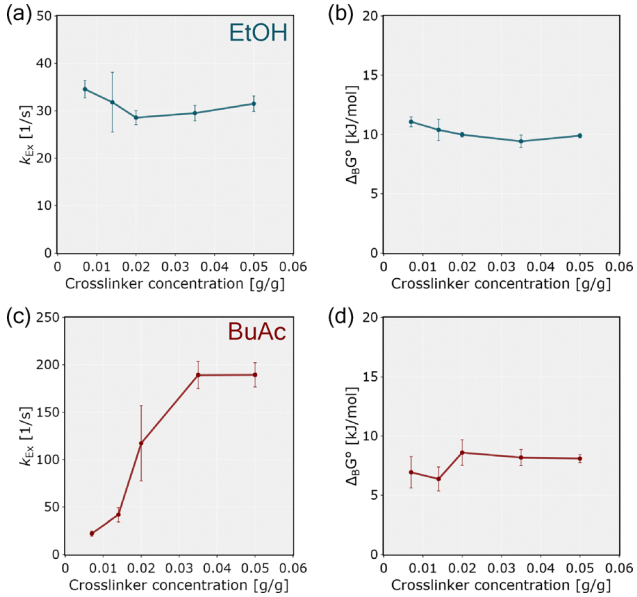

Fig. 9 Solvent exchange rate (k_{ex}) and standard Gibbs energy of binding ($\Delta_B G^\circ$) from free to bound state of pNIPAM in EtOH ((a) and (b)) and from restricted to bound state of pNIPAM in BuAc ((c) and (d)).

intended for qualitative interpretation; for a more comprehensive understanding, they should be complemented with further methods such as molecular dynamics simulations.

In the context of solvent exchange rate analysis, higher solvent exchange rates were observed mainly in BuAc compared to EtOH, indicating faster exchange between restricted and bound states, and lower kinetic barriers within the pNIPAM polymer network (Fig. 9a and c). This observation is consistent with the weaker solvent–polymer interactions predicted by COSMO-RS simulations. In contrast, EtOH exhibited lower solvent exchange rates, reflecting stronger binding affinities and increased kinetic limitations.

When examining the standard Gibbs energy of binding, the results provide only limited scope for a direct comparison between EtOH and BuAc. A lower $\Delta_B G^\circ$ was observed in BuAc, suggesting a stronger thermodynamic affinity for the polymer side chains, likely the hydrophobic isopropyl groups of pNIPAM, shaped by the polymer's steric environment (Fig. 9b and d). In contrast, the moderately higher $\Delta_B G^\circ$ in EtOH may result from limited access to the amide groups, which serve as primary binding sites and are located within hydrophobic domains.

These results reveal fundamental differences in solvent–polymer interactions. In BuAc, simulation model reveals weaker thermodynamic binding, while experimental measurements demonstrate faster solvent exchange between the two sites, together indicating rapid exchange between the different binding states of the solvent within network. The solvent molecules solvating the polymer chains are continuously replaced due to these accelerated exchange rates, leading to changes in the solvation states of the chains, ultimately resulting to structural collapse and gel shrinkage. In EtOH, on the other hand, stronger

binding and slower exchange occur due to its higher hydrogen-bonding potential and the restricted access to binding sites imposed by the polymer's steric environment, thereby stabilizing the lyogels in a swollen state. As has been concluded in earlier works,[11,28,57] our findings further emphasize the need to balance thermodynamic affinity and steric accessibility when designing lyogels with tailored transport properties and responsive behavior.

3.4. Proposed solvent–polymer interaction model

Based on these experimental findings, a mechanistic model of solvent–polymer interactions for pNIPAM in EtOH and BuAc is proposed (Fig. 10). In EtOH, strong hydrogen bonding with the amide groups facilitates solvent binding to the polymer side chains. In contrast, BuAc binds preferentially to the hydrophobic isopropyl groups and exhibits strong surface interactions with the polymer backbone. Structurally, pNIPAM in EtOH exhibits network swelling and the formation of macropores, while in BuAc a more compact structure with reduced porosity is observed. At equilibrium in EtOH, slow solvent exchange rates are indicative of strong solvent–polymer interactions, which support the formation of a stable solvation layer around the polymer backbone and side chains. This stabilizing effect contributes to preserve the gel's structural integrity. In contrast, BuAc exhibits fast exchange, which limit the formation of such a solvation layer. As a result, the polymer matrix experiences reduced solvation and increased structural contraction, ultimately leading to shrinkage of the lyogel network.

NMR relaxometry and diffusometry provide molecular level evidence for these behaviors, revealing fundamental differences in solvent–polymer interactions between EtOH and BuAc, which represents solvents of differing polarity. While a high-polarity solvent promotes swelling through slower exchange kinetics and side-chain binding limitation, a low-polarity solvent induces shrinkage due to rapid exchange and enhancing surface interactions.

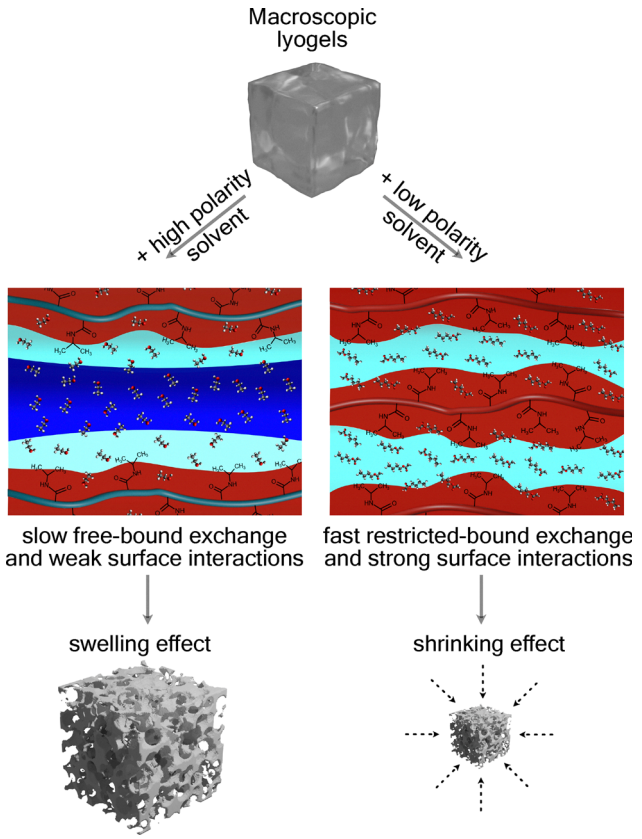

Fig. 10 Schematic representation of the proposed solvent–polymer interaction model, illustrating distinct solvent populations within pNIPAM lyogels in EtOH (high-polarity solvent) and BuAc (low-polarity solvent). The color scheme distinguishes the solvent states: bound solvent (red), restricted solvent (cyan), and free solvent (blue). Lyogels in EtOH exhibit a pronounced presence of free solvent, evidenced by a T_2 population near $\approx$1 s, characteristic of a swelling behavior. In contrast, BuAc does not show a detectable free solvent signal in this range, likely due to a faster solvent exchange rate that promotes gel shrinkage. Lyogels in EtOH exhibit weaker surface interactions (liquid-like) compared to BuAc, suggesting a more expanded pore structure. On the other hand, the stronger surface interactions (solid-like) observed in BuAc are associated with reduced pore volume and increased structural compaction.

4. Conclusions

This study demonstrates the effectiveness of combining NMR relaxometry and diffusometry with complementary techniques such as macroscopic swelling analysis and SEM imaging to investigate the microstructural dynamics of pNIPAM lyogels in solvents of varying polarity. In these systems, solvent polarity critically influences solvent–polymer interactions, exchange kinetics, and network morphology. EtOH, a high-polarity solvent with strong hydrogen bond energy, binds primarily to the amide groups, inducing swelling and macropore formation through slower solvent exchange. In contrast, BuAc, a low-polarity solvent, binds to hydrophobic isopropyl groups and exhibits faster solvent exchange, leading to a denser network, stronger surface interactions, and greater confinement.

These contrasting behaviors illustrate the importance of balancing thermodynamic affinity, kinetic accessibility, and steric factors when designing lyogels for targeted performance. This work not only deepens our understanding of solvent–polymer interactions but also provides insight into the structural and steric properties relative to bulk models, while highlighting NMR as a powerful tool for guiding the design of responsive soft materials for applications in dynamic chemical environments. These findings elucidate the interplay between molecular-scale dynamics, network structure, steric constraints, and thermodynamic binding, offering new insights into lyogel responsiveness and enabling rational design of materials for adaptive applications, including flow control and process intensification in functionally adaptable-tunable reactors. In future work, ultra-fast NMR measurement approaches can be implemented to overcome conventional timing limitations and enable the characterization of dynamic confinement behavior and rapidly evolving lyogel microstructures that remain inaccessible with standard acquisition methods.

Author contributions

Muhammad Adrian: conceptualization, data curation, formal analysis, investigation, visualization, writing – original draft, writing – review & editing. Kathrin Marina Eckert: conceptualization, data curation, formal analysis, investigation, writing – review & editing. M. Raquel Serial: conceptualization, formal analysis, supervision, writing – review & editing. Artyom Tsanda: conceptualization, writing – review & editing. Lukas Rennpferdt: resources. Stefan Benders: conceptualization, supervision, writing – review & editing. Hoc Khiem Trieu: funding acquisition. Tobias Knopp: funding acquisition, writing – review & editing. Irina Smirnova: funding acquisition, writing – review & editing. Alexander Penn: funding acquisition, supervision, writing – review & editing.

Conflicts of interest

There are no conflicts to declare.

Data availability

Data for this article, including Python scripts are available at https://doi.org/10.15480/882.16324.

The data supporting this article are included in both the main text and the supplementary information (SI). Supplementary information is available. See DOI: https://doi.org/10.1039/d5cp04032a.

Acknowledgements

This project is funded by the Deutsche Forschungsgemeinschaft (DFG, German Research Foundation) – SFB 1615 – 503850735. The authors gratefully acknowledge valuable discussions with Johannes Gmeiner. This paper was copy-edited with the assistance of the AI technology ChatGPT (v5.0) in order to improve clarity and readability. The authors have thoroughly checked all the proposed edits and take full responsibility for the content of this manuscript.

References

1 A. Richter, D. Kuckling, S. Howitz, T. Gehring and K.-F. Arndt, *J. Microelectromech. Syst.*, 2003, **12**, 748–753.
2 G. Gerlach, M. Guenther, J. Sorber, G. Suchaneck, K.-F. Arndt and A. Richter, *Sens. Actuators, B*, 2005, **111**, 555–561.
3 X. Hu, J. Karnetzke, M. Fassbender, S. Drücker, S. Bettermann, B. Schroeter, W. Pauer, H.-U. Moritz, B. Fiedler and G. Luinstra, *et al.*, *Chem. Eng. J.*, 2020, **387**, 123413.
4 X. Hu, C. Spille, M. Schlüter and I. Smirnova, *Ind. Eng. Chem. Res.*, 2020, **59**, 19458–19464.
5 T. Tanaka, *Phys. Rev. Lett.*, 1978, **40**, 820.
6 Y. Li and T. Tanaka, *J. Chem. Phys.*, 1990, **92**, 1365–1371.
7 T. Tanaka and D. J. Fillmore, *J. Chem. Phys.*, 1979, **70**, 1214–1218.
8 T. Tanaka, L. O. Hocker and G. B. Benedek, *J. Chem. Phys.*, 1973, **59**, 5151–5159.
9 T. Tanaka, I. Nishio, S.-T. Sun and S. Ueno-Nishio, *Science*, 1982, **218**, 467–469.
10 R. Yoshida, K. Uchida, Y. Kaneko, K. Sakai, A. Kikuchi, Y. Sakurai and T. Okano, *Nature*, 1995, **374**, 240–242.
11 T. R. Hoare and D. S. Kohane, *Polymer*, 2008, **49**, 1993–2007.
12 N. A. Guziewicz, A. Best, B. Perez-Ramirez and D. Kaplan, *Biomaterials*, 2011, **32**(10), 2642–2650.
13 T. Tanaka, D. Fillmore, S.-T. Sun, I. Nishio, G. Swislow and A. Shah, *Phys. Rev. Lett.*, 1980, **45**, 1636.
14 S. Hirotsu, Y. Hirokawa and T. Tanaka, *J. Chem. Phys.*, 1987, **87**, 1392–1395.
15 H. G. Schild, *Prog. Polym. Sci.*, 1992, **17**, 163–249.
16 K. M. Eckert, S. Müller, G. A. Luinstra and I. Smirnova, *Fluid Phase Equilib.*, 2024, **586**, 114182.
17 K. Poschlad and S. Enders, *J. Chem. Thermodyn.*, 2011, **43**, 262–269.
18 A. Rege, *Adv. Eng. Mater.*, 2023, **25**, 2201097.
19 K. M. Eckert, J. Bonsen, A. Hajnal, J. Gmeiner, J. Hasse, M. Adrian, J. Karsten, P. A. Kißling, A. Penn and B. Fiedler, *et al.*, *Fluid Phase Equilib.*, 2025, 114462.
20 B. Fu, H. Luo, F. Wang, G. Churu, K. Chu, J. C. Hanan, C. Sotiriou-Leventis, N. Leventis and H. Lu, *J. Non-Cryst. Solids*, 2011, **357**, 2063–2074.
21 P. Gupta, K. Vermani and S. Garg, *Drug Discovery Today*, 2002, **7**, 569–579.
22 M. Jaspers, A. C. H. Pape, I. Voets, A. E. Rowan, G. Portale and P. Kouwer, *Biomacromolecules*, 2016, **17**(8), 2642–2649.
23 A. Abragam, *The principles of nuclear magnetism*, Oxford university press, 1961.
24 P. T. Callaghan, *Principles of nuclear magnetic resonance microscopy*, Clarendon press, 1993.
25 E. O. Stejskal and J. E. Tanner, *J. Chem. Phys.*, 1965, **42**, 288–292.
26 R. Cotts, M. Hoch, T. Sun and J. Markert, *J. Magn. Reson.*, 1989, **83**, 252–266.
27 K. Saalwächter, *Prog. Nucl. Magn. Reson. Spectrosc.*, 2007, **51**, 1–35.
28 J. M. Giussi, M. I. Velasco, G. S. Longo, R. H. Acosta and O. Azzaroni, *Soft Matter*, 2015, **11**, 8879–8886.
29 E. V. Silletta, M. I. Velasco, C. G. Gomez, M. C. Strumia, S. Stapf, C. Mattea, G. A. Monti and R. H. Acosta, *Langmuir*, 2016, **32**, 7427–7434.
30 W. S. Price, *Concepts Magn. Reson.*, 1997, **9**, 299–336.
31 J. Kärger, M. Avramovska, D. Freude, J. Haase, S. Hwang and R. Valiullin, *Adsorption*, 2021, **27**, 453–484.
32 B. Maillet, R. Sidi-Boulenouar and P. Coussot, *Langmuir*, 2022, **38**, 15009–15025.
33 C. D'Agostino, R. Liuzzi, L. F. Gladden and S. Guido, *Soft Matter*, 2017, **13**, 2952–2961.
34 C. D'Agostino, V. Preziosi, C. Schiavone, M. V. Maiorino, G. Caiazza and S. Guido, *Soft Matter*, 2025, **21**, 3022–3029.
35 M. Knörgen, K.-F. Arndt, S. Richter, D. Kuckling and H. Schneider, *J. Mol. Struct.*, 2000, **554**, 69–79.

36 R. Serial and F. Jaureguialzo Zahnd, *Spinsolveproc*, 2025, DOI: 10.5281/zenodo.17079446.
37 P. D. Teal and C. Eccles, *Inverse Probl.*, 2015, **31**, 045010.
38 C. R. Vogel, *Inverse Probl.*, 1996, **12**, 535.
39 P. T. Callaghan, *Translational dynamics and magnetic resonance: principles of pulsed gradient spin echo NMR*, Oxford University Press, 2011.
40 X. Du, Y. Li, Y.-L. Xia, S.-M. Ai, J. Liang, P. Sang, X.-L. Ji and S.-Q. Liu, *Int. J. Mol. Sci.*, 2016, **17**, 144.
41 J. S. Jiménez and M. J. Bentez, *Biophysica*, 2024, **4**, 298–309.
42 K.-J. Dunn, D. J. Bergman and G. A. LaTorraca, *Nuclear magnetic resonance: Petrophysical and logging applications*, Elsevier, 2002, vol. 32.
43 W. Jencks, *Proc. Natl. Acad. Sci. U. S. A.*, 1981, **78**(7), 4046–4050.
44 M. Popovic, *Microb. Risk Anal.*, 2022, **22**, 100231.
45 T. Canal and N. A. Peppas, *J. Biomed. Mater. Res.*, 1989, **23**, 1183–1193.
46 A. Klamt, *J. Phys. Chem.*, 1995, **99**, 2224–2235.
47 V. M. Gun'ko, I. N. Savina and S. V. Mikhalovsky, *Gels*, 2017, **3**, 37.
48 H. Sugiyama, K.-i Katoh, N. Sekine, Y. Sekine, T. Watanabe and T. Ikeda-Fukazawa, *Chem. Phys. Lett.*, 2024, **856**, 141655.
49 M. D. Hanwell, D. E. Curtis, D. C. Lonie, T. Vandermeersch, E. Zurek and G. R. Hutchison, *J. Cheminf.*, 2012, **4**, 17.
50 P. McDonald, J.-P. Korb, J. Mitchell and L. Monteilhet, *Phys. Rev. E: Stat., Nonlinear, Soft Matter Phys.*, 2005, **72**, 011409.
51 C. D'Agostino, J. Mitchell, M. D. Mantle and L. F. Gladden, *Chem. – Eur. J.*, 2014, **20**, 13009–13015.
52 N. Bloembergen, E. M. Purcell and R. V. Pound, *Phys. Rev.*, 1948, **73**, 679.
53 D. Weber, J. Mitchell, J. McGregor and L. F. Gladden, *J. Phys. Chem. C*, 2009, **113**, 6610–6615.
54 K. Washburn, C. Eccles and P. Callaghan, *J. Magn. Reson.*, 2008, **194**, 33–40.
55 J. C. Gore, M. S. Brown, J. Zhong, K. F. Mueller and W. Good, *Magn. Reson. Med.*, 1989, **9**, 325–332.
56 L. G. Linck, S. A. M. Ochoa, M. Ceolin, H. Corti, G. A. Monti, F. V. Chávez and R. H. Acosta, *Microporous Mesoporous Mater.*, 2020, **305**, 110351.
57 M. C. Koetting, J. T. Peters, S. D. Steichen and N. A. Peppas, *Mater. Sci. Eng., R*, 2015, **93**, 1–49.

